August 7, 2001

Double Loop Configuration of a Flaring Region from Microwave, EUV and X-ray Imaging Data

M. R. Kundu[1], V. V. Grechnev[1,2,3], V. I. Garaimov[1], S. M. White[1]

[1] *Astronomy Department, University of Maryland, College Park, MD 20742*

`kundu,grechnev,gvi,white@astro.umd.edu`

[2] *Institute of Solar-Terrestrial Physics, Lermontov St. 126, Irkutsk, Russia 664033*

ABSTRACT

We use extensive multi-wavelength data to study a flare belonging to the interacting-loop class of events identified by Hanaoka. The class of flares is identified morphologically from the presence of two well-separated radio sources in 17 GHz images (in this event, 160″ apart), with only one source showing soft X-ray emission. This event shows many of the other properties apparently shared by this class of flares: a gradual rise showing many subsidiary peaks in both radio and hard X-ray light curves with a quasi-oscillatory nature, the presence of a bright compact X-ray emitting loop in the main flare source, a delay of the radio emission from the remote source relative to the main X-ray-emitting source, higher circular polarization in the radio emission of the remote source than in the main source, and stronger photospheric magnetic field in the remote source. The new results of our analysis are that we are able to show, using a sequence of magnetograms, that the magnetic field in the main flare site changes sharply at the time of the flare, and further we argue that the remote site is magnetically connected to the main flare site only up to the time of the main impulsive phase, at which point we believe the magnetic connection to the remote site was broken and further flare manifestations are largely confined to the main flare site. This severing of the magnetic connection between two well-separated active regions may be an intrinsic part of the energy release in this flare. The region around the main flare site also exhibits rotation in the magnetogram in the period leading

---

[3] V. V. Grechnev stayed at Nobeyama Radio Observatory as a Foreign Research Fellow of the National Astronomical Observatory of Japan

up to the flare. Radio and hard X-ray oscillations with periods of order 5 - 10 s are observed in the rise phase of this event. If they are due to transverse oscillations of the flare loop at the Alfvén speed, then the density in the loop is inferred to be of order 10^{11} cm^{-3} and to increase with time as expected.

Subject headings: Sun: flares – Sun: corona – Sun: radio radiation

1. INTRODUCTION

It has been known for a long time that flares occur in regions consisting of many magnetic loops. The multiple magnetic loop configuration of flaring regions has led to the suggestion that at least in some cases a flare is caused by the interaction between loops. Interactions between newly emerging flux and overlying magnetic fields have been known to cause flares (e.g. Zirin 1983; Kurokawa 1989). A two-dimensional reconnection model of such flares was developed by Heyvaerts et al. (1977) and it has been used in the past to interpret the onset of flares in various spectral domains (e.g. Kundu et al. 1982; Machado et al. 1988). Using Hα and magnetogram observations of (inferred) separatrices between interacting bipoles, Mandrini et al. (1991) and Demoulin et al. (1993) provided good evidence that interaction of bipoles could be essential to cause flares. Along the same lines, several authors (e.g. Hanaoka 1994; Inda-Koide et al. 1995; Shimizu et al. 1994) have shown that interactions between coronal loops as exhibited by Yohkoh Soft X-ray Telescope (SXT) observations can cause both flares and microflares. In the radio domain, only a limited number of observations of interacting flaring loops exist, primarily because of the lack of spatial resolution in the radio domain which is good enough to demonstrate the existence of such interacting loops.

In the past, Kundu et al. (1982) and Kundu & Shevgaonkar (1985) used VLA observations of two flares observed at 5 and 15 GHz with a few arcsecond spatial resolution, and interpreted the intensity and polarization maps of the flaring regions in terms of reconnection between newly emerging flux and the pre-existing flux or overlying magnetic field. More recently, Hanaoka (1996, 1997, 1999a) analyzed a relatively large number of flares using Nobeyama Radioheliograph (NoRH) data along with Yohkoh SXT and Kitt Peak Natioanl Observatory magnetogram data. He found that emerging flux appeared near one sunspot-dominated active region, and argued that the interactions between this emerging flux and the overlying loop resulted in the onset of flares and microflares, although he did not have magnetogram data available with sufficient cadence to test this idea thoroughly. The main flare site in each case was the location of emerging flux, which also happened to be the site of enhanced soft X-ray brightening. The NoRH images showed that at 17 GHz a compact brightening occurred at the main flare site as well as a brightening near a remote region of opposite polarity. Hanaoka (1999b) further showed that the 17 GHz brightenings in the remote sources (separated from the main flare sites by about 10^5 km) were delayed by some fractions of a second, implying that high energy electrons produced at the main flare site propagated over to the remote site. In addition, Hanaoka showed that microflares and jet-like plasma flows also occurred in similar magnetic field configurations. Silva et al. (1996) also observed a flare in which two well-separated sources brighten in the radio, with only one of the sources subsequently showing a bright compact soft X-ray loop. In that event, the radio images were acquired with the Very Large Array at 5 GHz.

In this paper, we discuss a solar flare which exhibits a similar magnetic field topology. The flare produces activity in two active regions separated by a large distance (10^5 km). The main flaring region (i.e., the region of the most intense emission at EUV, X-ray and radio wavelengths) contains a compact loop. We use data from a large number of sources: ground-based data from Nobeyama Radio Observatory and space data from the satellites SOlar and Heliospheric Observatory (SOHO), Yohkoh, and the Transition Region and Coronal Explorer (TRACE) to study this example of a flare involving both large and small loop systems and address the issues of how the two loop systems interact and what the possible triggers of the interaction are. In addition, this event features oscillations in X-ray and radio emissions which provide an additional constraint on physical parameters. High-cadence magnetogram data allow us to confirm the presence of changes in the magnetic field prior to the flare, and we are also able to show that the magnetic connection from the main flare site to the remote site is broken during the flare.

2. THE OBSERVATIONS

The event of 1999 Oct. 25 occurred in the active region complex consisting of AR 8741 and AR 8739 at 06:28 UT. The regions were located in the SE quadrant of the Sun's disk, with AR 8739 to the north-west and AR 8741 to the south-east. The flare in question was of importance M1.7 on the GOES X-ray classification scheme. GOES recorded flare onset at 06:28:08 UT, with peak soft X-ray emission at 06:31:15 UT, and X-ray emission ending at $\sim$ 06:45 UT. During the impulsive phase, Yohkoh/SXT was pointed to a different target. SXT images were not available until near the end of the flare (from about 06:40 UT on) when half-resolution data exist. However, Yohkoh Hard X-ray Telescope (HXT) data were available from flare onset, including the impulsive phase.

The event was observed with the imaging Nobeyama RadioHeliograph (NoRH) at 17 and 34 GHz, and also with the non-imaging Nobeyama polarimeters (NoRP) at 1, 2, 3.75, 9.4, 17, and 34 GHz. The peak radio fluxes were 60, 60, 62, 144, 76 and 43 sfu respectively at these frequencies. The NoRH radio images were processed using the NRAO software package AIPS with time resolutions of 1–10 sec. Final maps were produced using uniform weighting, cleaned and self-calibrated. Circular restoring beams of $10''$ at 17 GHz and $6''$ at 34 GHz were used in the final images to emphasize spatial resolution rather than sensitivity. To study flux variations at high time resolution we also used 0.1 s maps produced at 17 GHz using the Fujiki programs and at 34 GHz using the Hanaoka programs at Nobeyama.

In a multi-wavelength study such as this, careful coalignment of images at different wavelengths is essential. We carried this out by comparison of features visible at different wavelengths. We thus confirmed that the offsets of the pointing positions from disk center in the SOHO, Yohkoh and TRACE images were good to within 1 or $2''$. It is known that the NoRH images can suffer from a shift between the large-scale disk emission and the small-spatial-scale features, so we used a preflare 17 GHz image to determine the positional information by carefully coaligning the small-scale bremsstrahlung emission from hot coronal plasma with full-resolution SOHO Extreme-ultraviolet Imaging Telescope (EIT) images of the same emission for four different active regions spread over the solar disk. We estimate the final coalignment of the 17 GHz images with respect to the EUV images to be good to within $5''$. Since the NoRH 34 GHz images can suffer from shifts as large as those at 17 GHz, we determined that the 34 GHz source morphology was consistent with the 17 GHz sources and shifted the 34 GHz images accordingly.

2.1. Time Profiles and Images

Figure 1 shows the time profiles of this event in all four HXT channels (L: 14–23 keV, M1: 23–33 keV, M2: 33–53 keV, H: 53–93 keV), and at 3 radio frequencies (9.4 GHz polarimeter data, 17 GHz and 34 GHz radioheliograph fluxes). The flare emission time profiles in both hard X-rays and microwaves are characterized by a slow rise to maximum from about 06:28:15 to 06:29:50 UT, on which many small spikes of emission are superposed. The impulsive phase (06:29:50–06:30:20 UT) at radio wavelengths is dominated by two sharp spikes which also seem to exist in all four HXT bands, with the second spike being much weaker than the first. The impulsive phase is followed by a decay phase lasting until about 06:45 at radio wavelengths; however, no hard X-ray emission was detected in the M1, M2, and H channels beyond 06:34 UT. There was an enhancement of radio emission during the period from 06:32:20 to 06:34:20 UT.

A magnetogram from the Michelson Doppler Imager (MDI) instrument on SOHO was obtained at 06:23:34 UT, just prior to the event. Half-resolution EIT 195 Å images (dominated by Fe XII emission and thus sensitive to plasma at temperatures of $(1-2) \times 10^6$ K) were taken under the CME Watch program every 12 minutes, at 06:24:11 in the preflare phase, and at 06:36:10 and 06:48:11 in the post-maximum phase. Figure 2 shows contours of the 17 GHz and 34 GHz I (total intensity) images superimposed on the EIT 195 Å image from 06:36 UT (Fig. 2a). Also shown are contours of the 17 GHz Stokes V (circularly polarized flux) map superimposed on the MDI magnetogram (Fig. 2b). The 17 GHz images show two sources (southern source in AR 8741 labelled A, and northern source in AR 8739 labelled B) separated by 160″, together with a third source (C) lying between them. The southern radio source A is close to a compact loop observed to lie near the leader spot in AR 8741 in the EIT 195 Å image at 06:36 UT (this loop is not apparent in Fig. 2a due to saturation of the color table which was chosen to emphasize the weak loops connecting the two active regions; the loop can be better seen in Figure 3). The compact loop is about 15″ long. The apparent peak brightness temperature of this source measured in the radio maps is $T_{B\,max} = 1.8 \times 10^7$ K at 17 GHz and 3.4×10^6 K at 34 GHz. The northern radio source B lies over the sunspot at the trailing edge of AR 8739 ($T_{B\,max} = 2.4 \times 10^6$ K). The 17 GHz V-maps along with the MDI magnetogram indicate that we are dealing with a large loop connecting the two ARs together with a small compact loop in AR 8741. The 34 GHz images show emission only from the compact loop in AR 8741. The trailing sunspot in AR 8739 has a strong magnetic field (longitudinal field in excess of 1500 G in the MDI magnetograms), while the magnetic fields in the vicinity of the short EUV flare loop at source A range from −1100 to 700 G.

Yohkoh/HXT observed this event in all 4 channels (L, M1, M2, and H). There are sufficient counts to construct images in the L channel throughout the event, whereas in the M1 and M2 channels images can only be made at times near the flare peak. In Figure 3 we present images in several HXT channels at different times overlaid on the 06:36 UT EIT 195 Å image of the main flare loop at source A. For comparison, we also include the NoRH images of the radio emission at source A in Figure 3 (lower panels). At the beginning of the event (06:29:04 UT) the HXR source in the M1 & M2 bands consists of two components, which seem to lie near the footpoints of the compact EIT flaring loop. It is clear that at flare maximum (06:29:54) the strongest HXR emission comes from the western footpoint of the EUV loop in all HXT bands. However, during the onset (06:29:04), the HXT/L source is located over the eastern footpoint and it subsequently spreads over the western footpoint. At the time of the maximum hard X-ray emission (06:29:54 UT) the left footpoint shows only weak L-band emission whereas the right footpoint is much stronger. After the X-ray maximum, the L-band source seems to occupy the entire flaring loop (06:31:59 UT). Later in the post-maximum phase the L-band emission consists of only one source which seems to be located near the top of the compact EIT loop (06:32:59 UT). Unfortunately there were insufficient counts in the M1, M2 or H channels to investigate light curves for the different footpoint and looptop sources in order to determine whether they show correlated emission. The radio images are consistent in size and orientation with the EIT and HXR flare emission; the 34 GHz image in particular shows a loop very similar to the loop in the EIT image.

As mentioned earlier, Yohkoh/SXT images of the region are not available until 06:40 UT when half-resolution images were taken, so we only have images of the hot plasma in the decay phase. During this phase the radio images at 17 GHz show, in addition to those present in the impulsive phase, a third source (source C in Fig. 2a) coinciding with a feature in the EUV images. The post-flare loops are shown in Figure 4. Fig. 4a presents the SXT image at 06:40 UT overlaid with 17 GHz I-contours from the average of all 17 GHz source maps made during the post-maximum period 06:30:40–06:36:00 UT in order to enhance the low-level features, and shows the relative locations of the three sources at 17 GHz in the decay phase of the event: source C clearly lies near the middle of the long flare loop visible in the SXR image. Figure 4b shows a comparison of the MDI magnetogram (gray scale) with contours of the SXR image (at 06:40 UT) and HXR images overlaid. Fig. 4c shows the EIT 195 Å image at 06:48 UT in gray scale overlaid by the same contours of SXR and HXR. The HXR contours are of the M1 band from 06:29:06 – 06:29:14, in the rise phase of the event, while the H band contours are from 06:29:52 – 06:29:58, at the peak of the HXR emission. The H band contour shows that the highest–energy HXR photons detected by HXT at the peak of the flare come predominantly from one footpoint (the western footpoint) of the EIT loop, consistent with Fig. 3. Fig. 4c shows that the 17 GHz source C also corresponds reasonably well with faint flare emission observed in the EUV. Note that there is no strong corresponding feature in the magnetogram (Fig. 4b) at the location of this source: there are several positive-flux features in this area, but the magnetic field strength lies everywhere in the range of -20 to $+100$ G. The EUV images show compact discrete features in this region before the flare, and they are then seen to brighten during the flare.

Radio source C is obviously thermal in nature and associated with post-flare soft X-ray emitting loops: it has a gradual rise phase, its brightness temperature does not exceed 2×10^5 K, and it is unpolarized. In this phase it is probably located near the SXR loop top.

2.2. Magnetic Connectivity Between the Active Regions

In order to understand the magnetic connection between AR 8739 and 8741 and its possible role in the flare, we have studied images of the region from EIT (Fe IX/X 171, Fe XII 195 Å & Fe XV 284 Å full resolution images at about 07:06 UT, with 2.6″ pixels), TRACE 171 Å images at high cadence ($0\rlap{.}''5$ pixels; the images cover AR 8739 but not AR 8741) and the post-flare SXT images ($4\rlap{.}''9$ pixels). Figures 2 and 4 show soft X-ray and EIT 195

Å images, while Figure 5 shows four selected TRACE 171 Å images taken from the high-cadence sequence observed during the event. The 171 Å passband is dominated by lines of Fe IX and X, i.e. by plasma at around 1×10^6 K.

As can be seen in Fig. 4a, there are two possible magnetic connections between AR 8741 and AR 8739. During flare decay the brightest set of loops in the soft X-ray images are the sharply curved and possibly sigmoid-shaped western set of loops connecting the southern part of the trailing end of AR 8739 with the western side of the leading spot of AR 8741 (source A) in the post-flare phase via source C. In addition there are fainter loops which are straight in projection and connect the east side of source A to source B at the eastern edge of AR 8739. Both sets of loops are evident in SXT images acquired about an hour before the flare and show roughly equal brightness at that time. The TRACE and EIT EUV images also show the straighter loops which connect AR 8741 and AR 8739 more directly, but these loops do not show any strong response to the flare in the EUV images. By contrast the TRACE 171 Å images show strong flows of cool gas along the direction of the sigmoidal SXT loops, which we infer to be the remnants of hot gas from the loops visible in SXT which has radiatively cooled. All EUV images show small discrete stationary features in the region of the post-flare loops and radio source C. An Hα image at 06:31 UT from the Solar Flare Telescope of NAOJ at Mitaka in Japan (provided by T. Sakurai, NAOJ) also shows bright emission at source C with a morphology very similar to that of the TRACE 171 Å image at 06:36 UT, in addition to strong Hα emission from the vicinity of the main flare loop at source A. The discrete features in the TRACE 171 Å images look like a collection of compact low-lying loops (Figure 5), but if they are discrete compact loops then it is difficult to understand why they brighten as a result of the remote flare since there should be no way for nonthermal electrons produced in the main flare site to gain access to those compact loops. We assume instead that they mark the footpoints of loops connecting source A to source C, and are visible because hot plasma on these loops cools into the 171 Å range at the footpoints because of higher densities there. The presence of Hα emission at sources A and C is additional evidence that these are the locations of the footpoints of loops connecting the two sites.

2.3. Magnetic Evolution of the Pre-Flare Region

There was good coverage by MDI for two days prior to and including the pre-flare, main flare, and post-flare phases with a cadence of about 96 minutes (Figure 6). From this data we found that both AR 8741 and 8739 evolved rather gradually in magnetic field strength. Inspection of a magnetogram movie shows rotation of the magnetic field in the vicinity of the main flare site in AR 8741. To show these changes with stationary images, in Figure 6 we present a sequence of magnetograms for the leader part of AR 8741, where the main flare site is located, and use crosses to provide stationary reference points (Fig. 6a-h, two upper rows). These points are marked by numbers in the first frame (Fig. 6a). The figure covers an interval of $\simeq$ 22 hours spanning the flare, from Oct. 24, 11 UT through Oct. 25, 09:35 UT. Solar rotation, including the differential component, has been removed from these images. Inspection of the sequence of images shows most of the magnetic features in the leading part of AR 8741 moving with respect to the fiducial points.

Two enlarged frames are shown in the lower panels. Fig. 6i shows the magnetogram taken on Oct. 24 at 07:59 UT, and Fig. 6j shows the magnetic field just before the flare, on Oct. 25 at 06:23. The latter magnetogram is also superimposed onto the earlier one in the left image (Fig. 6i) to reveal the changes. Contour levels are -330 and 200 G (30% of the minimum and maximum values). White lines with arrows show the displacements of some prominent features between the two magnetograms.

We investigated several global characteristics of the magnetograms such as the average strength of the magnetic field, for each magnetic polarity separately, the area occupied by magnetic fields whose strength exceeds a certain value (e.g., 100 G), and maximum and minimum values of the field strength. These characteristics were studied separately for both AR 8741 and 8739 as well as for their leader and follower parts. Two effects can be seen. There was a monotonic increase of the maximum magnetic field of N-polarity in the follower part of both regions, from 700 G on Oct. 24 (00:00 UT) to 1300 G on Oct. 26 (00:00 UT) for AR 8741 and from 1120 G to 1620 G for AR 8739. Further, the positive flux in AR 8741 showed a sharp increase just prior to the flare. In Figure 7a and b we show variations of the positive and negative magnetic flux over the main flare site (indicated in Fig. 6j by the dashed frame). The positive flux, associated with the small positive pole, increased sharply just prior to the flare, as is evident in Figure 6g, and then decreased again afterwards. There was no counterpart in the negative polarity to balance this peak.

2.4. Radio Emission

In the impulsive phase 17 GHz radio emission is observed from both southern (i.e., source A in Figure 1) and northern (source B in Figure 1) sources which are separated by $160''$. The NoRH maps allow us to study the time variability of both sources separately. These two sources seem to lie near the footpoints of large loops that connect the two AR's (as exhibited by the SXT image in the post-maximum phase and by EIT images during the maximum). Both 17 GHz sources have a simple source structure, but the southern source appears to be spatially extended whereas the northern source is more compact. 34 GHz I-maps show that emission at this frequency comes only from the southern source, which had a maximum flux of 40 sfu. The upper limit to the 34 GHz flux from the northern source is about 3 sfu. The locations and shapes of the southern radio sources are consistent with the compact EIT loop (Fig. 3). The 17 GHz circular polarization maps (Stokes V) show that the north source is highly (steady at around 65%) right circularly polarized (RCP) while the southern 17 GHz source is predominantly left circularly polarized (LCP), with a much lower degree of polarization (steady at $\sim$ 15%, with no structure corresponding to the fine structure in the light curves). The high-resolution images indicate that the southern source has a very weak right circularly-polarized component on the north-west edge of the main LCP V source (Fig. 2b and Fig. 3, lower panels), but we infer that the separation of the two oppositely-polarized components is too small to be resolved with the $10''$ beam at 17 GHz. The northern source at 17 GHz is actually extended in the inferred direction of the loop connecting it to the main flare site, as may be seen from the outer contour in Fig. 2b.

In order to determine the deconvolved sizes of the radio sources we have fitted single elliptical gaussians convolved with the clean beam size to sequences of 17 and 34 GHz images. At 17 GHz, the southern source has a size of order $10'' \times 8''$ with a position angle of $120° \pm 20°$ measured east of north. At 34 GHz, the southern source has dimensions of $12'' \times 8''$ at a position angle of $130° \pm 30°$. Thus the southern source has a similar orientation at both 17 and 34 GHz, but the 34 GHz source appears to be larger even though the resolution is better there. The size and orientation of both are consistent with the loop observed in the EIT 195 Å image at 06:36 UT (Fig. 3). The remote northern source at 17 GHz is smaller than the southern source, with dimensions of $9'' \times 5''$ at a position angle of $0° \pm 10°$. We interpret the larger size of the southern source at 34 GHz compared to 17 GHz as being an optical depth effect: if the 34 GHz source is dominated by emission from the two footpoints of the loop whereas the 17 GHz source is brighter at the top of the loop than at the footpoints because it is (at least marginally) optically thick at the lower frequency, then the 17 GHz source will appear smaller even though the emission comes from the same loop.

The rise phase of the burst is characterized by a steady exponential growth with a rise time τ of order 16 s starting approximately at 06:28:57 and lasting until 06:29:11 (over 3.5τ), onto which quasi-periodic oscillations are superimposed. The oscillations are also observed in hard X-rays, but they are not as pronounced there. The period of oscillations is initially 6.0 s and then gradually increases to about twice this value. We discuss them further in the next section.

In Fig. 8 we compare the time profiles of flux from the northern and southern sources at 17 GHz. As one can see, most of the radio emission originates from the southern source, with the first peak of radio emission at 06:29:09 UT. The flux of the northern source was less than 20% of the maximum flux of the southern source. Comparison of the time profiles at 17 GHz for the southern and northern sources shows that these profiles have similar time structure before the event maximum (06:29:50 UT), but later they show major differences: as the southern source reaches its maxima in the two spikes at the peak of the impulsive phase, the northern radio source is declining. This suggests that during the rise phase the radio emission is produced by nonthermal electrons which are generated in AR 8741 and gain access to the long loops which connect to AR 8739; this connection is terminated at the time of the two spikes and the electrons accelerated after that time no longer have access to the long loops, so the trapped electrons in those loops then decay.

The spectral maximum is around 10 GHz during the peak of the burst. The overall high-frequency spectral index is about -1 during the main peak, indicating nonthermal emission. This emission is dominated by the southern source. On closer inspection it can be seen that the two strong spikes at 06:30 UT have a relatively steep spectrum (-1.5 to -2.0) while the more gradually varying component has a flatter spectrum (less than -1). The emission from the northern source is clearly dominated by the steep-spectrum spiky component and the upper limit to the 34 GHz flux there (about 3 sfu) is consistent with the peak 17 GHz flux of 9 sfu and a spectral index of -1.5 to -2. After about 06:30:40 the overall spectrum is essentially flat at high frequencies, indicating that thermal bremsstrahlung dominates the radio emission. This is consistent with the similarity between the radio and EUV images after this time, and the close match between the bremsstrahlung radio flux predicted from the GOES data (Figure 1) and the 17 and 34 GHz fluxes in the decay phase.

3. THE OSCILLATIONS

Analysis of the time profiles of emission of this event shows that during the rise phase of the flare there seem to exist oscillations in both hard X-ray and microwave bands (see Fig. 1). For detailed studies of these oscillations, we removed the smoother background emissions. In Figure 9 we present the time profiles of the oscillatory emissions in the HXT bands and at 17 GHz. We note that the profiles are similar in three HXT channels (L, M1, M2). We have calculated the correlation coefficients between the emissions in different HXT channels, and between HXT channels and 17 GHz. We find that the coefficients of correlation are 0.92, 0.84, 0.58 and 0.77 between the HXT L and M1 channels, HXT M1 and M2 channels, HXT L channel and 17 GHz south source, and HXT M1 channel and 17 GHz south source respectively. These relatively large coefficients of correlation suggest that emissions in hard X-rays and at 17 GHz in the southern source are similar in nature and the same electron population is responsible for these emissions.

Oscillations may reflect the characteristic frequency of some structure in the corona and thus can be used to infer physical properties of coronal structures. In this event, there is the additional involvement of loops with two very different lengths, and the question of whether the oscillations appear on both loop systems. Since the oscillation period reflects a resonance in a particular structure, two structures with different sizes should have very different oscillation periods. The presence of the same oscillation period in large and small loops would imply that one structure is the source of the radiating particles in both sets of loops.

In Figure 10 we identify individual oscillation peaks, showing that the "period" of the oscillations grows with time. Oscillations visible simultaneously in microwaves and hard X-rays can be due to modulation of the magnetic tube width by a disturbance moving across the loop at the Alfvén speed. As noted earlier, the width l of the southern radio source is $8'' = 5.6 \times 10^3$ km at both 17 and 34 GHz. The average value of the magnetic field at the photosphere under this source is 280 G. If we know the coronal magnetic field B in the source, we can estimate the plasma density as a function of time by assuming that the interval between peaks is the time taken to cross the loop and return at the Alfvén speed 2.2 $\times$ 10^6 B/$\sqrt{n}$ km s^{-1}. The result is shown in Fig. 10 for assumed field strengths of 150 and 200 G. The inferred density rises with time because the interval between peaks increases as the flare proceeds. Taking the height of the cylindrical source to be equal to its diameter, we obtain the emission measure of this volume (Fig. 10, lower panel). We note that all these estimates depend greatly on the values of the magnetic field and the size of the source ($n \propto B^2/l^2$, EM $\propto B^4/l$), which are not known accurately, so the quantitative estimates are coarse. In Fig. 10 we plot values for assumed magnetic fields of 150 and 200 G to illustrate the dependence on B.

We can compare this result with the estimates from soft X-ray data. Unfortunately we have no SXT data until late in the event, so we rely on GOES data to infer the temperature and emission measure of the hot plasma. Using the volume assumed above (a cylinder of diameter and height both 5.6×10^3 km) which is appropriate for the compact loop observed in the radio and EUV images, we obtain a density of 4×10^{11} cm^{-3} at the peak of the soft X-ray emission (GOES EM = 2×10^{49} cm^{-3}, T = 1.5×10^7 K), and about 3×10^{11} cm^{-3} at the time of the last peak in Fig. 10 (GOES EM = 1.5×10^{49} cm^{-3}), so the density inferred from the oscillations is consistent with the soft X-ray data to within the (large) uncertainties.

4. DISCUSSION

4.1. Flare Configuration

The flaring source consisted of two regions separated by 10^5 km. These two regions were clearly magnetically connected as seen from their opposite polarities and the similarity of the microwave time profiles at 17 GHz, as well as by the soft X-ray and EUV-emitting material between the two regions. The main flare location shows a compact flare loop. In the beginning of the flare, the easternmost footpoint of this loop was illuminated by hard X-rays, and then the brightness center in HXR shifted to the right (western) foot point of the new small loop. One possible scenario is that the left footpoint, in a region of downgoing magnetic flux, is initially connected to upgoing flux in the remote site in AR 8739 via a long loop, and then reconnects to the closer site of upgoing flux in AR 8741 as a result of the flare.

Hanaoka (1996) suggested that in this class of flares newly emerging flux interacts with overlying pre-existing loops and triggers a reconnection process responsible for the flare energy release. This emerging flux scenario is a possible interpretation for this event since we clearly see increases in the magnetic flux around the time of the event (Fig. 7). However, it is also known that other types of photospheric motions, for example, shear motion, can also provide pre-flare energy storage. We see from the set of magnetograms in Fig. 6 that the leader part of AR 8741 experienced a rotational motion. The rotating region was rather compact, $\sim 50'' \times 50''$. The surrounding region of photosphere was steady and did not exhibit any rotation. Thus we expect that a shear increasing with time will be generated along the boundary of the rotating region. The velocity of the rotation on the periphery reaches 100 m s^{-1}. For the small region of S-polarity (black just below the white feature in Fig. 6b, point #2), which was driven towards the N-polarity region and then pushed away leftwards (Fig. 6d-g), the velocity was ~ 2 times higher. The rotational motion of the S-polarity magnetic flux in the leader region of AR 8741 toward the compact N-polarity feature may produce a twist in the coronal magnetic structure. We suggest that a reconnection process can start due to the pressure of new magnetic flux tubes on the pre-existing magnetic configuration not only from below but also from the side. In this case, newly formed configurations become tangled and bent, and can form bizarre structures such as the sigmoid-like post-flare SXR loop connecting AR 8741 and AR 8739.

Sigmoids are believed to be precursors of eruptive events since they indicate the presence of extreme twists in the magnetic field prior to its emergence from the convection zone. The statistics given by Canfield et al. (2000) shows that in most cases the presence of sigmoids in active regions correlates well with manifestations of eruptions. However, there are cases when sigmoids were observed with no eruptions. In our case we are possibly dealing with a similar "pseudo-sigmoid": the observed coronal configuration had temporarily a sigmoid-like shape, but due to superficial deformation of the coronal structure rather than emergence of twisted ropes. In this case the sigmoid-like configuration quietly relaxed, and no activity (at least, no flares) was observed in AR 8741 after this flare until November 1.

4.2. Hard X-ray and Microwave Emissions

Non-thermal emissions in hard X-rays are detectable starting from the time of the trigger of HXT (06:29:06 UT), and they essentially cease after 06:30:10. The power-law photon spectral index is between 3.5 and 4.0, and under the assumption of thick-target precipitation the corresponding electron energy power-law spectral index $\delta \simeq 5$. This implies a microwave spectrum significantly steeper than was observed. Thus it again appears that the microwave-emitting electrons have a flatter spectrum than the hard X-ray-emitting electrons. Optical depth effects may also play a role in the apparent radio spectral index: if the 17 GHz emission is not optically thin as we assume then the true radio spectrum could in fact be steeper.

4.3. Connection Between the Main and Remote Sources

Inspection of Figure 8 indicates that, at least in the rise phase, the radio light curves of the main and remote sources behave similarly. In Figure 11 we plot a section of the 17 GHz light curve at 0.1 s resolution just prior to the main impulsive-phase peaks, for both the main southern source (dashed line, scaled) and the remote northern source. For display purposes we have delayed the light curve for the main source by 0.9 seconds relative to the remote source. Particularly between 06:29:38 and 06:29:48, the delayed light curve of the main source matches the light curve of the remote source in detail. However, a single value for the delay may not apply to the whole light curve.

This delay of the remote source is a clear indication that the nonthermal electrons producing the radio emission are accelerated in the main flare site and then propagate to the remote site along magnetic field lines. We follow Hanaoka (1999a) and use the 0.9 s delay of the remote source to estimate the electron energy. The measured distance between the sources is 1.2×10^5 km, giving an apparent velocity of 1.3×10^5 km s^{-1}, which is very close to the values deduced for several flares by Hanaoka (1999b). This velocity needs to be corrected for loop curvature (i.e., the difference between the projected length of the loop and its actual length: the correction factor ranges from $1 + \theta^2/24$ for a circular arc subtending an angle $\theta \ll 1$ to $\pi/2$ for a semicircular loop) and for the pitch angle distribution of the electrons. The latter correction is of order 1.23 for an isotropic pitch angle distribution (Hanaoka 1999b). Of the two sets of loops connecting AR 8741 and 8739 discussed in section 2.2, the direct loops connecting source A to source B would have a small correction for loop curvature whereas the sigmoid-shaped loop would have a larger correction. Unfortunately, we are unable to determine which set of loops is appropriate for the nonthermal electrons propagating from the main to the remote source because of insufficient accuracy in the overlays. The fact that the sigmoid-shaped loop is brighter in the decay phase suggests that more energy was deposited on those loops. To handle this uncertainty, we calculate an inferred electron velocity range corresponding to loop curvature corrections from 1 to $\pi/2$, i.e., velocities from 1.6 to 2.5 $\times$ 10^5 km s^{-1}, corresponding to kinetic energies from 90 to 410 keV. This is the typical energy range of hard X-ray producing electrons, and confirms that the interpretation of the delay as the time taken by energetic electrons to propagate freely along a magnetic field line to the remote site is plausible.

The presence of the delay confirms that the remote site is magnetically connected to the main site during the rise phase, and the main site is the location of electron acceleration. The new result of this investigation is evidence that this connection is terminated just as the main impulsive phase begins. The evidence is twofold: (i) even though the radio flux from the main source rises sharply, the flux level of the remote source drops after this time, indicating that no new nonthermal electrons are injected onto the field lines and we observe just the decay of the previously-injected electrons; and (ii) the light curves of the main and remote sources no longer show the same features with a delay. We cannot judge whether the fact that the "disconnection" of the remote site as the main site reaches its peak is significant or just a coincidence, but one possible scenario is that the most explosive energy release is triggered by a reconnection of field lines which initially connected negative polarity regions in AR 8741 to positive polarity regions of AR 8739 such that after the flare they connect to the positive polarity region in AR 8741 itself, as represented by the loop seen in the EIT 195 Å image at 06:36 UT. In this scenario, the energy release is driven by the need for AR 8741 to break a magnetic connection to the remote site in AR 8739 and reconnect instead to closer flux. We note that the light curve for the remote source still shows some fine structure superimposed on the decay after 06:29:50 UT, so this fine structure cannot be associated with the acceleration site in our interpretation. It could be due to instabilities in the population of electrons trapped on the loop following disconnection.

Figure 11 also indicates that the 34 GHz light curve of the southern source does not show the same degree of fine structure during the rise phase of the event as does the 17 GHz emission. This contrast suggests that two components contribute at 17 GHz: a steadily rising component with a flatter radio spectrum, and a quasi-oscillatory component with a steeper radio spectrum which contributes relatively less at 34 GHz. We noted earlier (section 2.4) that the spiky component of the radio emission seems to have a steeper spectrum than the overall radio emission. The images do not appear to show any morphological difference between these two components, if that is the correct interpretation. The 9.4 GHz light curve (Figure 1) also shows both components with much higher flux levels than at 17 or 34 GHz, suggesting that both are indeed nonthermal. If the steep-spectrum quasi-oscillatory component is confined to the long loop connecting the northern and southern radio sources, while the flatter-spectrum smooth component is due to harder-spectrum electrons trapped predominantly in the compact loop in the southern source, then we expect that 34 GHz emission will not be detected from the northern source due to the dominance of the steep-spectrum component there.

Finally, we note one peculiarity in the light curve of the northern remote source. If the radiating electrons are produced with a range of pitch angles and energies then the time taken to propagate from the main to the remote source will be different for different electrons, and we then expect the light curve for the remote source to be smoothed out relative to the main source, as well as delayed. However, at the time resolution of 0.1 s (one-tenth of the propagation time), we see no evidence for such smoothing. Specifically, from 06:29:44.0 to 06:29:45.5 we see two peaks and two troughs repeated in both 17 GHz light curves (see the inset in Fig. 11). If we smooth the light curve for the main source by a Gaussian function with a full-width at half-maximum of 0.2 s, we do not see these features. This implies that the electrons propagating to the remote source suffered a time dispersion of less than 0.2 s. This is difficult to understand unless the electrons are accelerated initially with a small range of velocities parallel to the magnetic field.

4.4. Comparison with Hanaoka's events

Since this is a complex event with many different aspects, it is worth summarizing the observations in the context of Hanaoka's analysis of this class of flares. The following properties observed in this event appear to be common to many events of this class (Hanaoka 1996, 1997, 1999a,b):

- The light curves show a relatively slow rise in both hard X-rays and microwaves.
- Both hard X-ray and radio light curves show many subsidiary peaks with a quasi-periodic separation.
- Radio images show two sources separated by a large distance: in this event, the two sources are in different active regions 160″ apart. Only one of the sources would be

identified as the flare site at other wavelengths (e.g., a bright loop is observed at the main flare site at EUV wavelengths). The remote source is not prominent at any other wavelength range (e.g., soft X-rays, EUV).

- Both radio sources show the oscillations.
- The magnetic field appears to be stronger at the remote source and the radio polarization is higher there than at the main flare site.
- The dominant radio polarizations in the main and remote sources are of opposite sense.
- The main radio source shows evidence of being bipolar.
- The radio emission from the remote source is delayed with respect to the main source, with the delay corresponding to apparent velocities of order $1 - 2 \times 10^5$ km s^{-1}.

It is striking that events selected on purely morphological grounds (two well-separated sources in the 17 GHz images, with only one showing bright X-ray emission; Hanaoka 1997) show so many similarities in other properties. We note that the selection based on the presence of two well-separated radio sources introduces a selection effect which favors a stronger magnetic field at the remote source: in any event where the remote source does not lie in a stronger field the radio emission from the remote source is probably not detectable at 17 GHz because the number of nonthermal electrons is lower in the remote source than in the main source, and they radiate less strongly because optically-thin gyrosynchrotron emissivity is proportional to a high power of the magnetic field strength (e.g., $\propto B^{3.4}$ for an E^{-4} energy distribution: Dulk & Marsh 1982).

5. CONCLUSIONS

1. The multiwavelength study of this impulsive flare has permitted us to clarify the manifestations and properties of multiple loop configurations of a complex flaring region. We suggest that the flare could be caused by an interaction of magnetic structures resulting from sideward motion of the coronal loops driven by quasi-rotational photospheric motions. The post-flare structure formed as a result of such an interaction has a sigmoid-like shape.

2. The microwave flaring source consists of two components separated by a large distance (over 10^5 km), the two component sources being located in AR 8741 and AR 8739. The radio emission of the main and remote sources show opposite senses of circular

polarization. Only the source at AR 8741 is identified as the main flare site because a bright loop is observed here in EUV and hard X-rays; by contrast, the remote source is not detected at EUV, soft X-ray or hard X-ray wavelengths. These properties are consistent with the remote radio source being produced by electrons which are accelerated in the main flare site and propagate $160''$ to the remote flare site where they produce radio emission in strong magnetic fields, but do not deposit a significant amount of energy by precipitation, either because too few electrons reach the remote site or else they mirror in the strong magnetic field there and do not precipitate at the remote site.

3. The radio flare structure consists of a long loop whose footpoints are separated by $160''$, and, in addition, a small loop which is the main flare site. This flaring structure is clearly a double-loop configuration of the type discussed earlier by Hanaoka. Hanaoka speculated that emerging flux triggered the interaction between the two loops, but did not have available magnetogram data with sufficient cadence to investigate this issue quantitatively. The magnetograms acquired every 96 minutes by SOHO/MDI allow us to show that indeed there is a change in magnetic flux in the main flare site just prior to this flare. However, another scenario is also possible in this event: the magnetogram sequence indicates that the photospheric magnetic fields rotated around the flare site, possibly producing sheared coronal structures which subsequently flared.

4. In addition to the main compact flare loop and the long loops connecting AR 8741 with AR 8739, this event exhibits another set of loops connecting the main flare site (source A) to source C. Flows along these loops in both directions are seen in TRACE 171 Å images, and Hα flare ribbons are detected at both ends of these loops. However, there is no evidence for nonthermal particles on this loop system in either the X-ray or radio data. The magnetic field at the western (source C) footpoints of these loops is weak.

5. During the rise phase of the flare, there seem to exist oscillations in both hard X-ray and microwave domains. The oscillations in the main flare at 17 GHz and in hard X-rays are similar in nature, implying that the same electron population is responsible for the emissions. Transverse oscillations of the main (compact) flare loop are a plausible source of these oscillations. However, they are also observed in the radio light curve of the remote source which is on a different loop: this implies that the injection of nonthermal electrons onto this loop is modulated by the oscillations in the main flare loop. The oscillation period allows us to determine the density in the flare loop under the assumption that the oscillation period corresponds to transverse oscillations of the loop at the Alfvén speed.

6. An important result of this study which has not previously been demonstrated is that the connection between the main flare site and the remote site is broken at the time of the main impulsive phase. At this time, the radio flux in the remote site begins to drop, rather than rise as it does in the main site; and the main and remote light curves cease to show the same structures with a delay as they do during the rise phase of the flare. This disconnection might be associated with field lines rooted in negative flux in AR 8741 (the main flare site) changing their connection from positive flux in the remote site in AR 8739 to positive flux in the main flare site. This implies that the flare is driven by the need for AR 8741 to simplify its magnetic connectivity, switching from long connections to AR 8739 to shorter connections within AR 8741 itself.

M. Kundu and V. Grechnev wish to thank the staff of NAOJ and NRO (Japan) for their help and hospitality during their stay at the observatories. We thank the referee for his perceptive comments which led to important improvements in the paper. This research at Maryland was supported by NSF grants ATM 96-12738, ATM 99-90809 and INT-98-19917, and NASA grant NAG 5-8192. This research was also partly supported by Russian *RFBR* grants No. 00-02-16819, 99-07-90038, 00-15-96710, *INTAS-RFBR* grant 97-02071033 (IR-1088), and the program *"Astronomy"*.

REFERENCES

Demoulin, P., Van Driel-Gesztelyi, L., Schmieder, B., Henoux, J.-C., Csepura, G., & Hagyard, M. 1993, A&A, 271, 292

Dulk, G. A. & Marsh, K. A. 1982, ApJ, 259, 350

Hanaoka, Y. 1994, ApJL, 420, L37

—. 1996, Solar Phys., 165, 275

—. 1997, Solar Phys., 173, 319

Hanaoka, Y. 1999a, in Nobeyama Symposium on Solar Physics with Radio Observations, ed. T. S. Bastian, N. Gopalswamy, & K. Shibasaki (Nobeyama Radio Observatory), 229

—. 1999b, PASJ, 51, 483

Heyvaerts, J., Priest, E. R., & Rust, D. M. 1977, ApJ, 216, 123

Inda-Koide, M., Sakai, J., Koide, S., Kosugi, T., Sakao, T., & Shimizu, T. 1995, PASJ, 47, 323

Kundu, M. R., Schmahl, E. J., Velusamy, T., & Vlahos, L. 1982, A&A, 108, 188

Kundu, M. R. & Shevgaonkar, R. K. 1985, ApJ, 292, 733

Kurokawa, H. 1989, Space Sci. Revs., 51, 49

Machado, M. E., Moore, R. L., Hernandez, A. M., Rovira, M. G., Hagyard, M. J., & Smith, J. 1988, ApJ, 326, 425

Mandrini, C. H., Demoulin, P., Henoux, J.-C., & Machado, M. E. 1991, A&A, 250, 54

Shimizu, T., Tsuneta, S., Acton, L. W., Lemen, J. R., Ogawara, Y., & Uchida, Y. 1994, ApJ, 422, 906

Silva, A. V. L., White, S. M., Lin, R. P., de Pater, I., Gary, D. E., McTiernan, J. M., Hudson, H. S., Doyle, J. G., Hagyard, M. J., & Kundu, M. R. 1996, ApJS, 106, 621

Zirin, H. 1983, ApJ, 274, 900

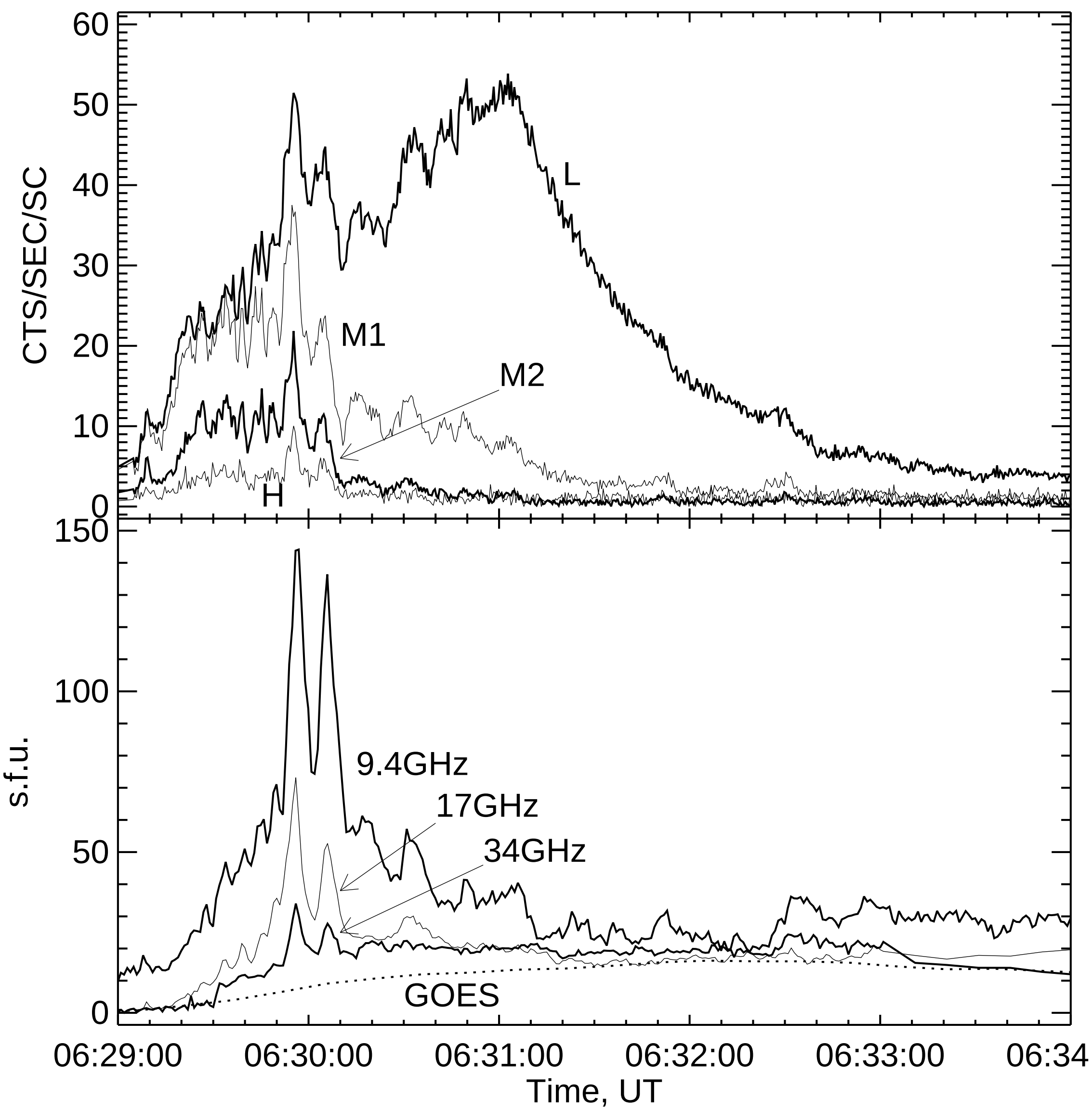

Fig. 1.— Time profiles of hard X-rays in all Yohkoh/HXT channels (upper panel: L, 14–23 keV; M1, 23–33 keV; M2, 33–53 keV; and H, 53–93 keV), as well as at the radio frequencies of 9.4, 17, and 34 GHz (lower panel). The 9.4 GHz data are from the Nobeyama polarimeter, while the 17 and 34 GHz data are from the radioheliograph. In addition, the lower panel shows the radio flux expected from thermal bremsstrahlung by the hot soft X-ray-emitting material detected by the GOES satellite.

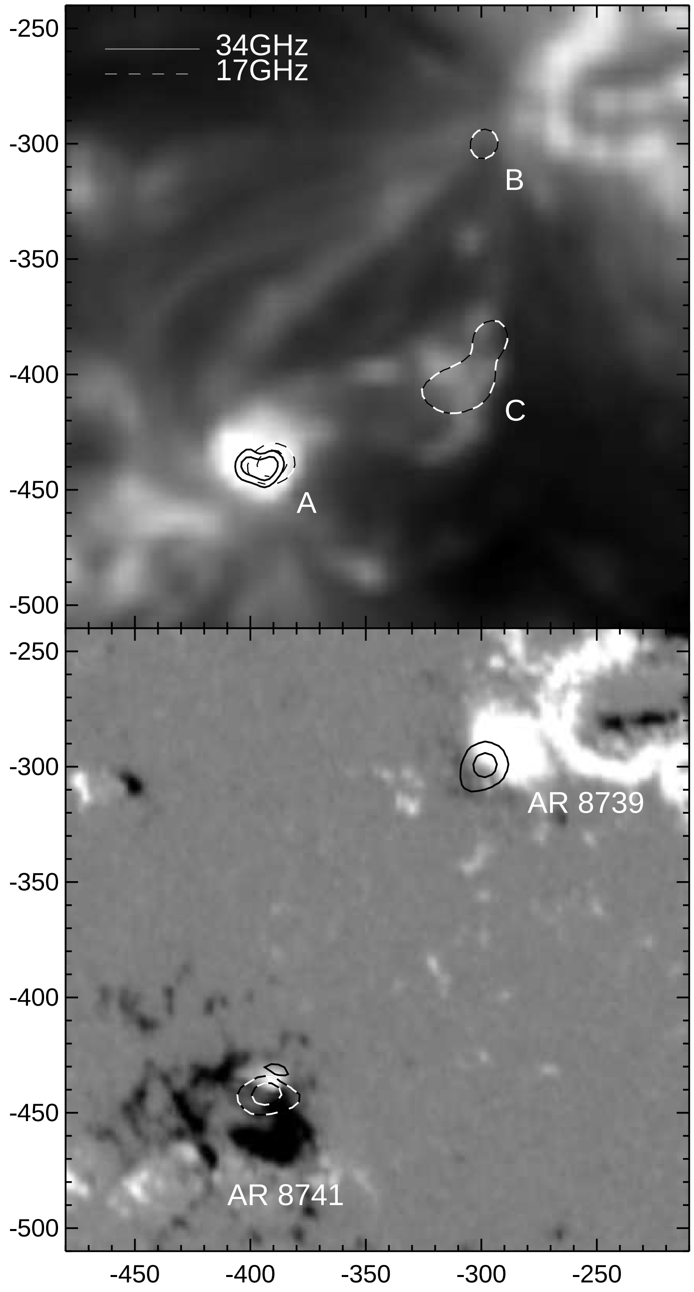

Fig. 2.— (a, upper panel) Contours of microwave Stokes I images (17 GHz, dashed and 34 GHz, solid) superposed onto the EIT 195 Å image taken at 06:36 UT. The radio image for the main (label A) and remote (label B) sources is taken at 06:29:45 UT, close to the peak of the flare, while the radio image for thermal source C which strengthens during the flare decay phase is taken at 06:32:05 UT. The spatial resolution of the radio data is $10''$ at 17 GHz and $6''$ at 34 GHz, while the EIT image has $5''.2$ pixels. The transfer function for the EIT image is chosen to emphasize the weak loops connecting the two active regions and the main flare loop at source A is saturated; it is shown unsaturated in Figure 3. (b, lower panel) Contours of the Stokes V (circular polarization) map at 17 GHz at 06:29:45 superimposed onto a magnetogram of the region acquired by SOHO/MDI at 06:23:34.

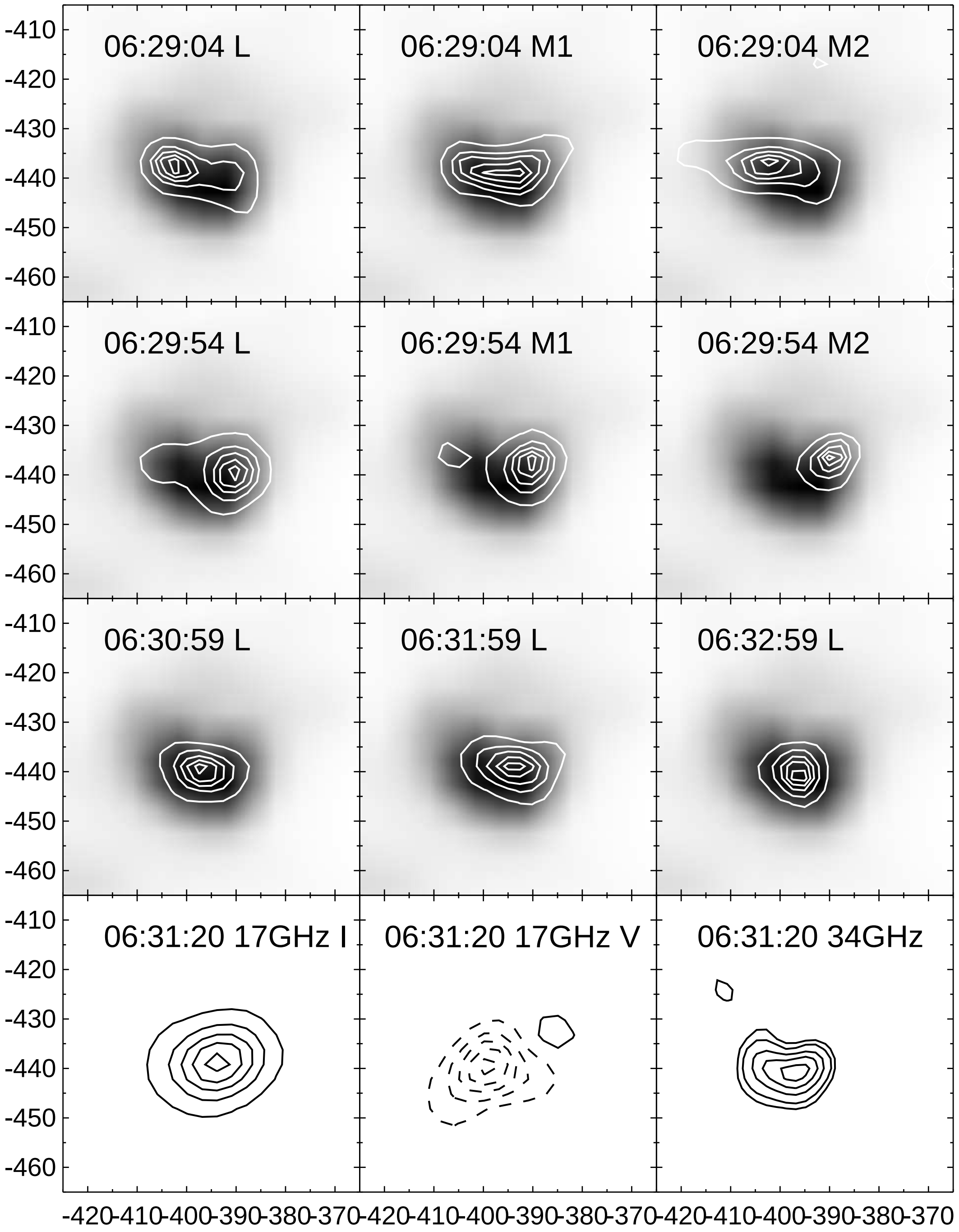

Fig. 3.— HXT contours (L, M1, and M2 bands) overlaid on the EIT 195 Å image of the flaring region (06:36 UT, halftone, negative transfer function showing the brightest emission). The EIT image has 5.″2 pixels. The contours show the L, M1, and M2 channels at 06:29:04 (upper row) and at 06:29:54 (second row), and the L channel at 06:30:59, 06:31:59, and 06:32:59 (third row). The panels in the bottom row show contours of the radio emission at 06:31:20 UT at 17 GHz (I and V) and 34 GHz, with the same field of view. Contours are at 10, 30, 50, 70 & 90% of the peak in each map, which is 2.9×10^6 K in the 17 GHz I map, -2.4×10^5 K in the 17 GHz V map, and 1.2×10^6 K at 34 GHz.

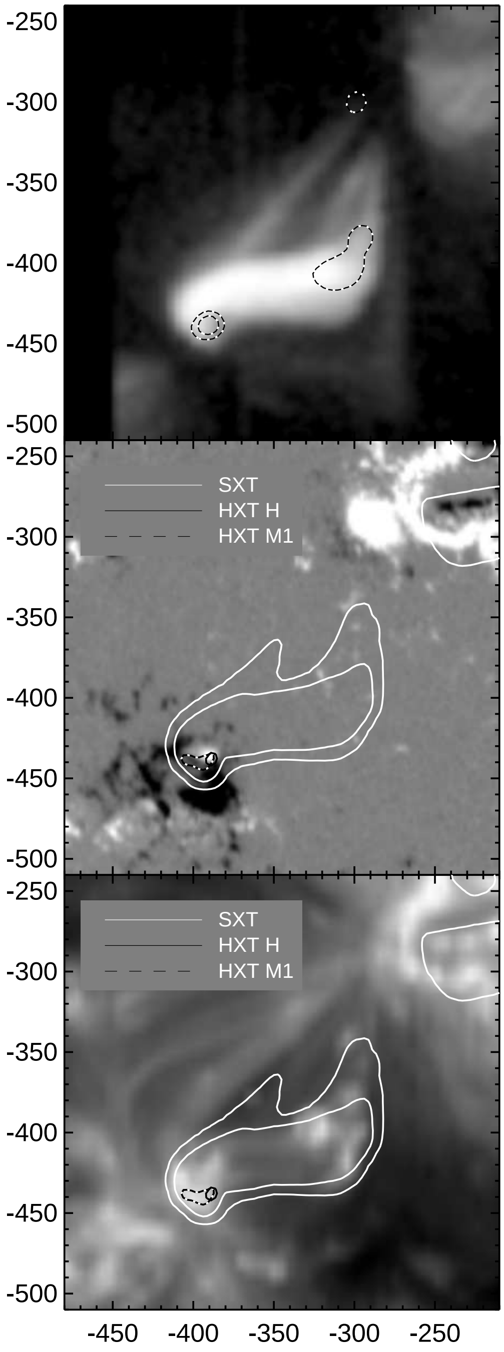

Fig. 4.— Images of the flare region from (a, upper panel) SXT composite image after the flare (halftone) overlaid with 17 GHz Stokes I contours at 06:32:25 UT. Three microwave sources are detected at this time: the two main footpoint-associated sources as well as an SXR looptop-associated thermal source. (b, middle panel) the MDI magnetogram at 06:23 UT, and (c, lower panel) the EIT 195 Å image at 06:48 UT (halftone), both overlaid with contours of the SXT image from 06:40 UT (white solid contours) and HXR images (dotted contour: M1 channel, 06:29:06 – 06:29:14; black solid contour: H channel, 06:29:52 – 06:29:58).

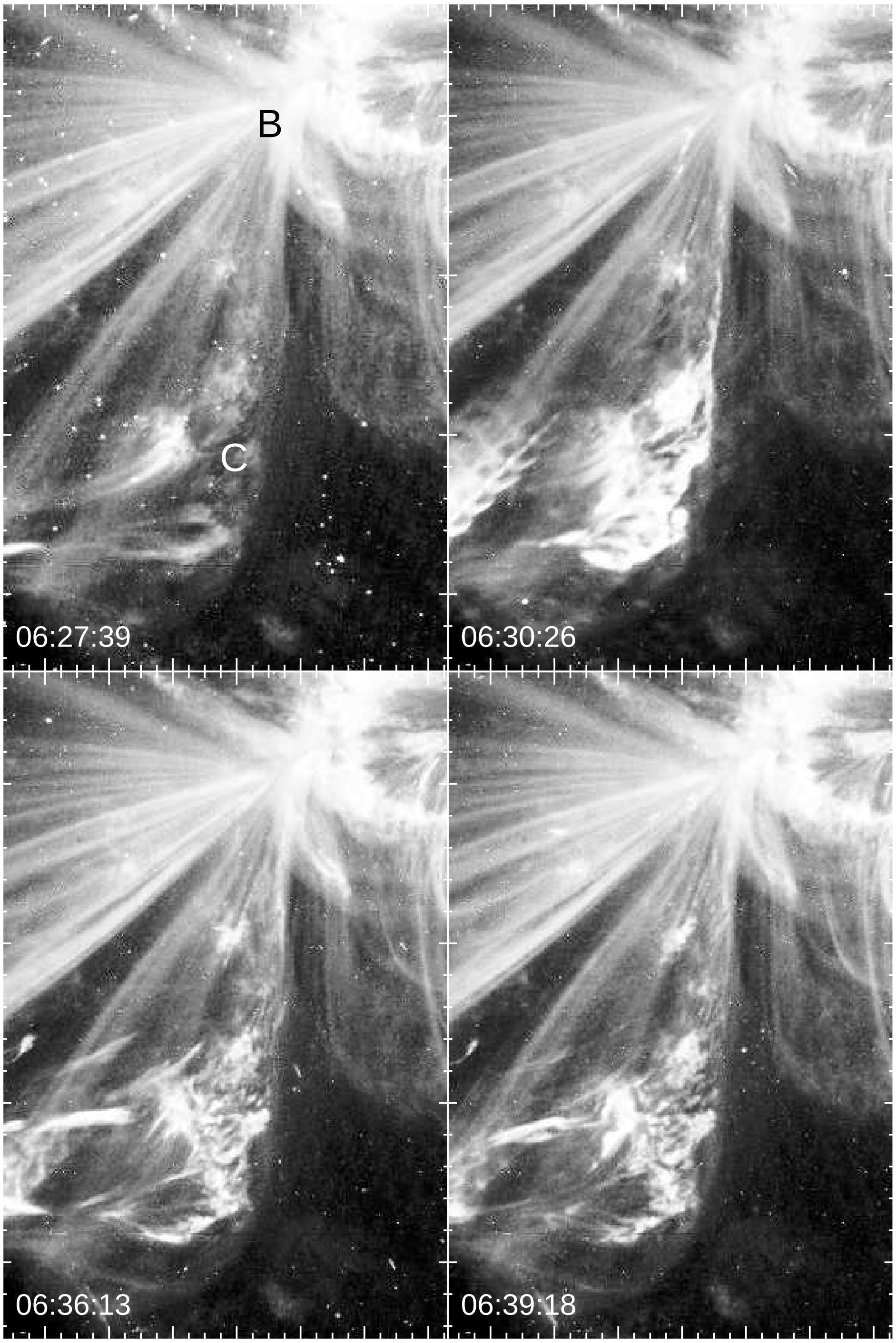

Fig. 5.— TRACE 171 Å images during the flare. The first image is prior to the impulsive phase. The TRACE field of view did not include the main flare site: diffraction spikes associated with bright impulsive phase emission there can be seen in the lower left side of the image at 06:30:26 UT. These images have a pixel size of $0\farcs5$.

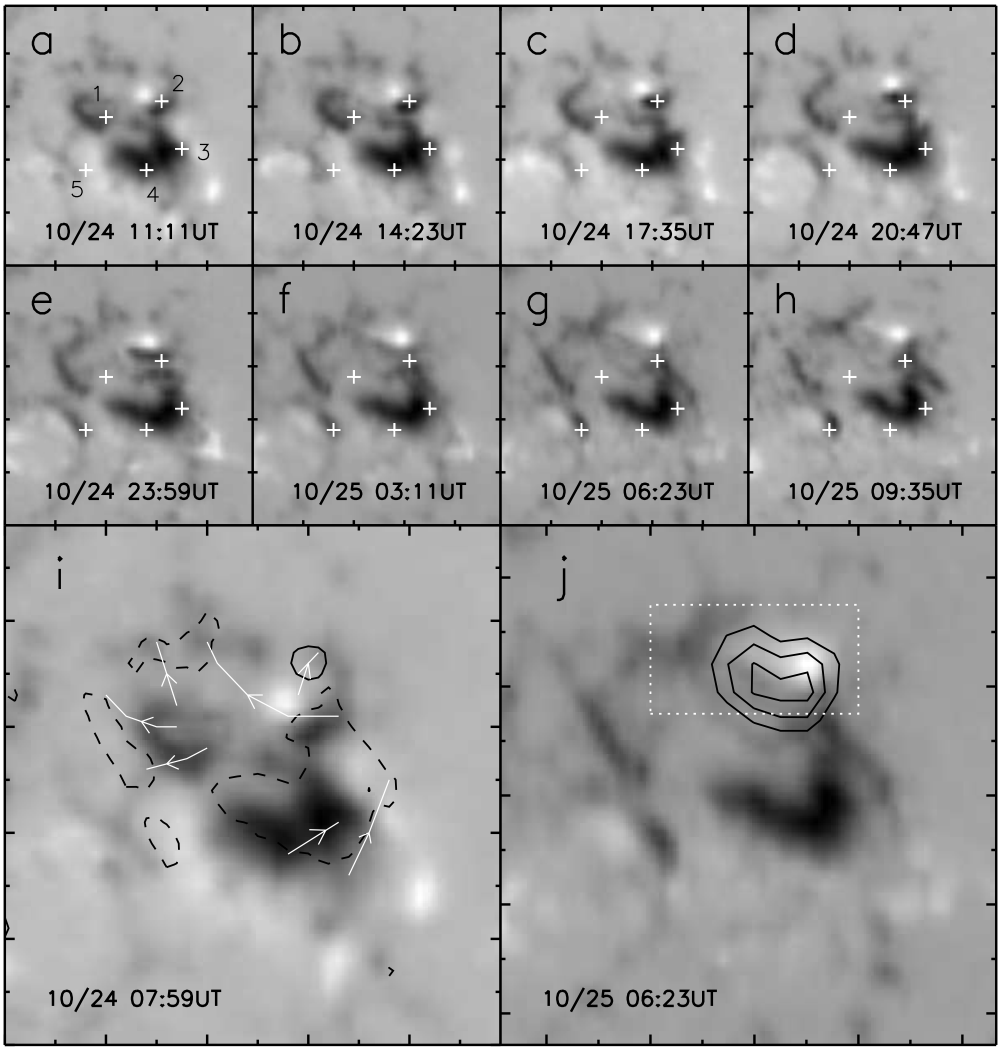

Fig. 6.— A set of magnetograms for the leader part of AR 8741 where the main flare site is located. (a–h) a sequence of the magnetograms from Oct. 24, 11 UT to Oct. 25, 09:35 UT. (i) magnetogram of Oct.24, 07:59 UT (halftone) overlaid by contours of the magnetogram of Oct. 25, 06:23 UT. White lines with arrows show the displacements of some prominent features in the magnetograms. (j) just before the flare, on Oct. 25 at 06:23, overlaid with contours of the small loop seen in the EIT image at 06:36 UT. The dotted white rectangle represents the area used for the magnetic field measurements shown in Fig. 7. White crosses in (a)–(h) represent fiducial reference points which can be used to look for changes in the magnetograms. Each panel is 98″ in size.

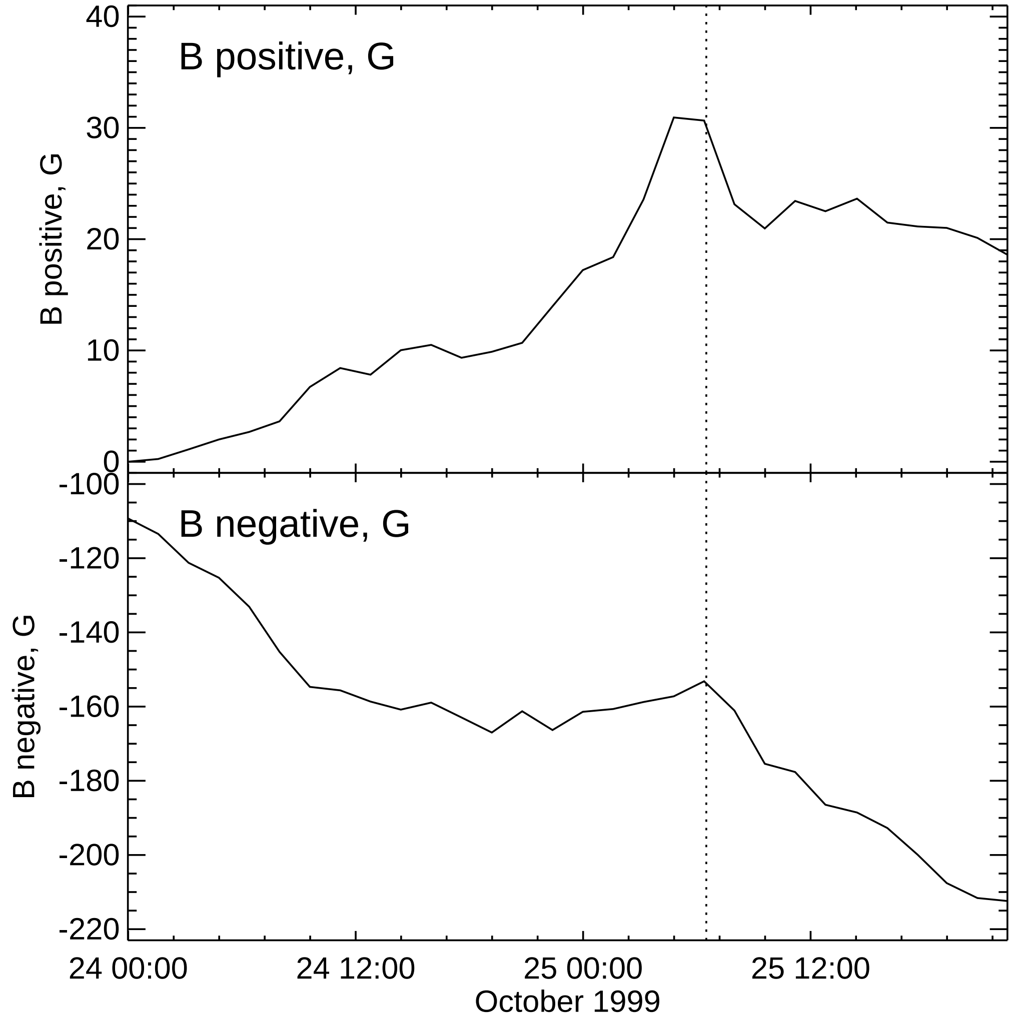

Fig. 7.— Variations of the magnetic flux averaged over the main flare site (the area shown in Fig. 6j by the dotted frame). (a, upper panel) magnetic flux averaged over pixels of only positive (North) polarity, (b, lower panel) the same for pixels of only negative polarity.

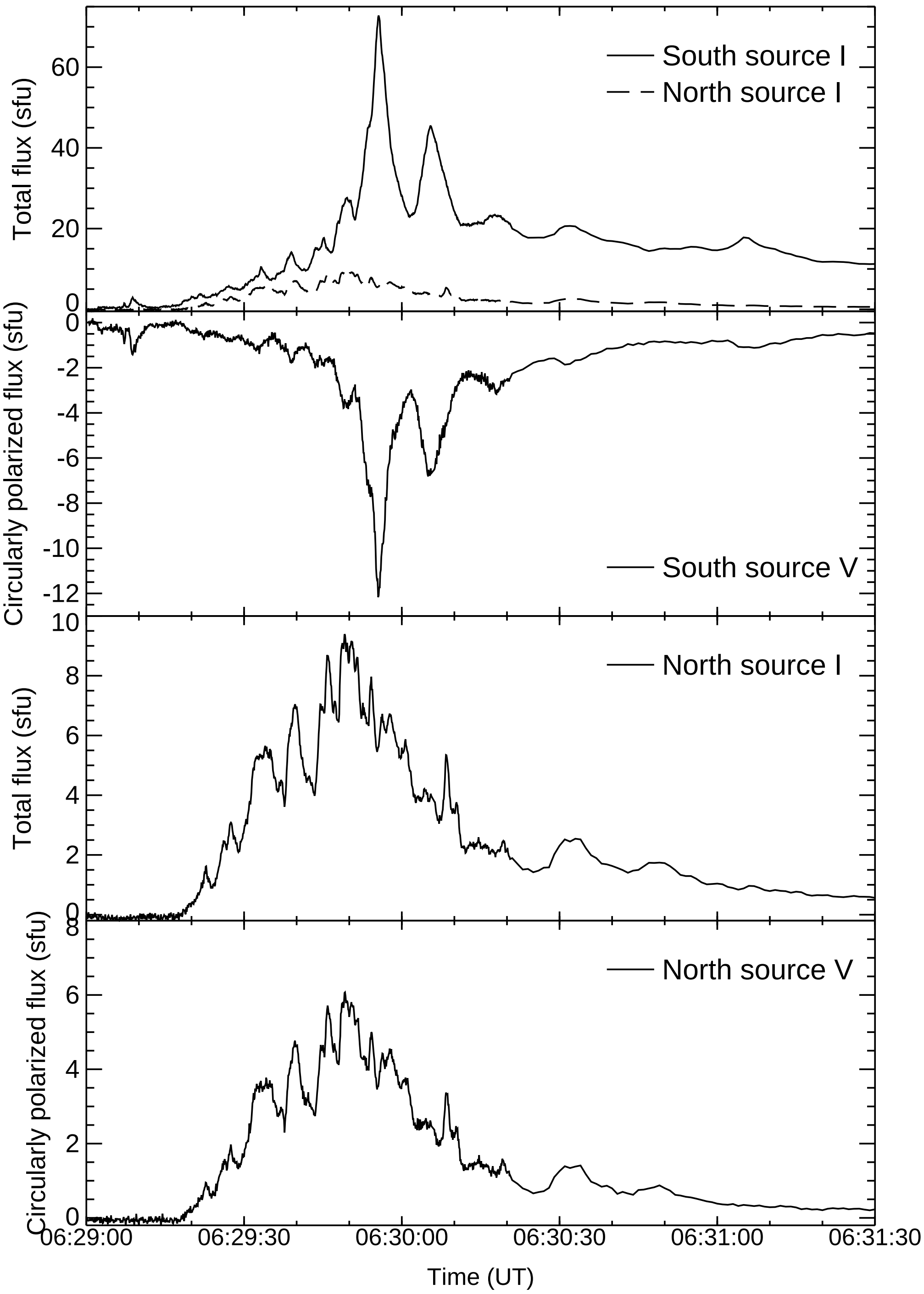

Fig. 8.— Time profiles of the total flux from the north (lower two panels) and south (upper two panels) sources at 17 GHz for Stokes I (first, third panels from top) and V (second, fourth panels from top). The time resolution is 0.1 s until 06:30:20 UT, when it reverts to 1.0 s.

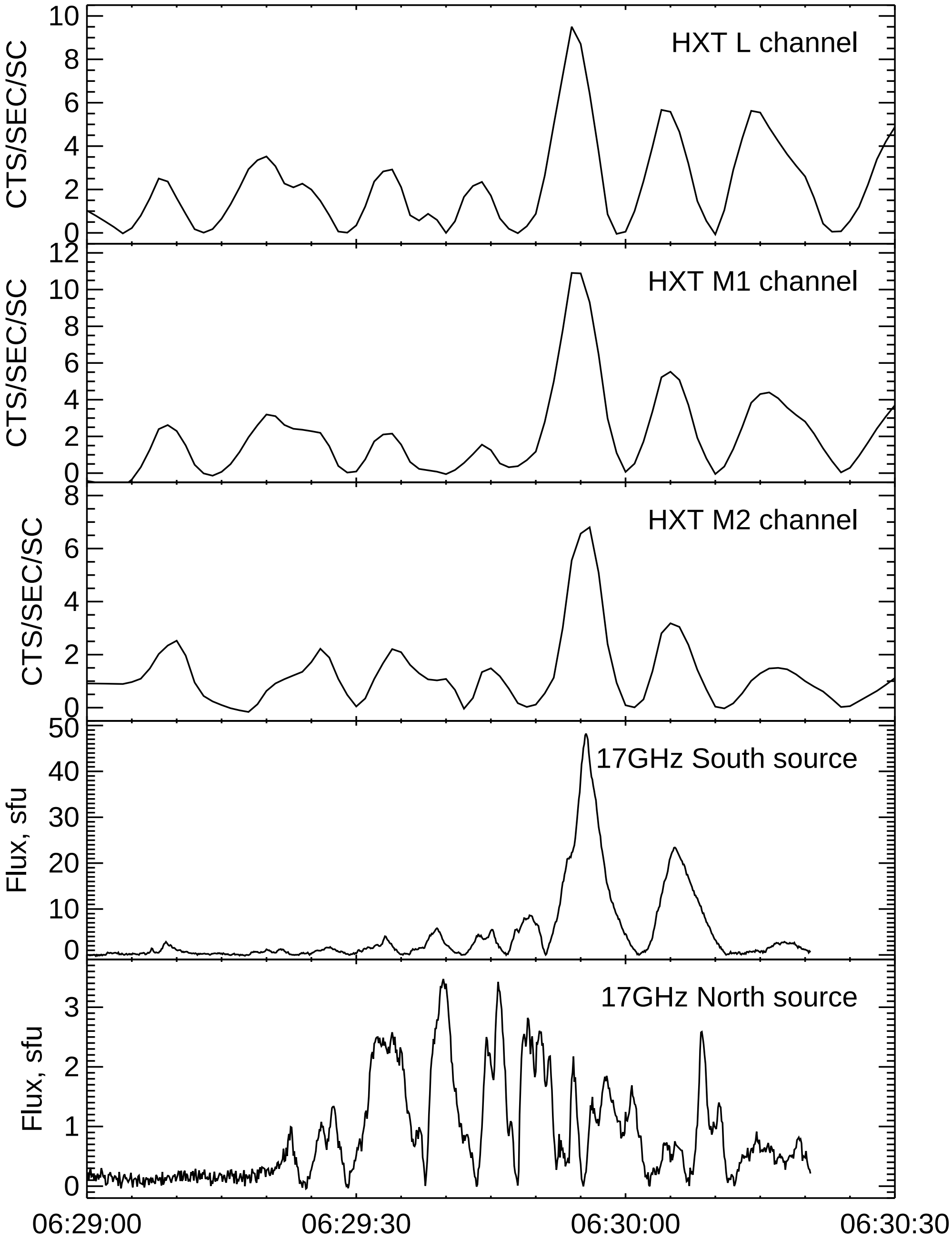

Fig. 9.— Filtered time profiles of the oscillatory emissions in HXT (L, M1, and M2 bands) and of the north and south sources at 17 GHz. A lower envelope has been removed from each light curve.

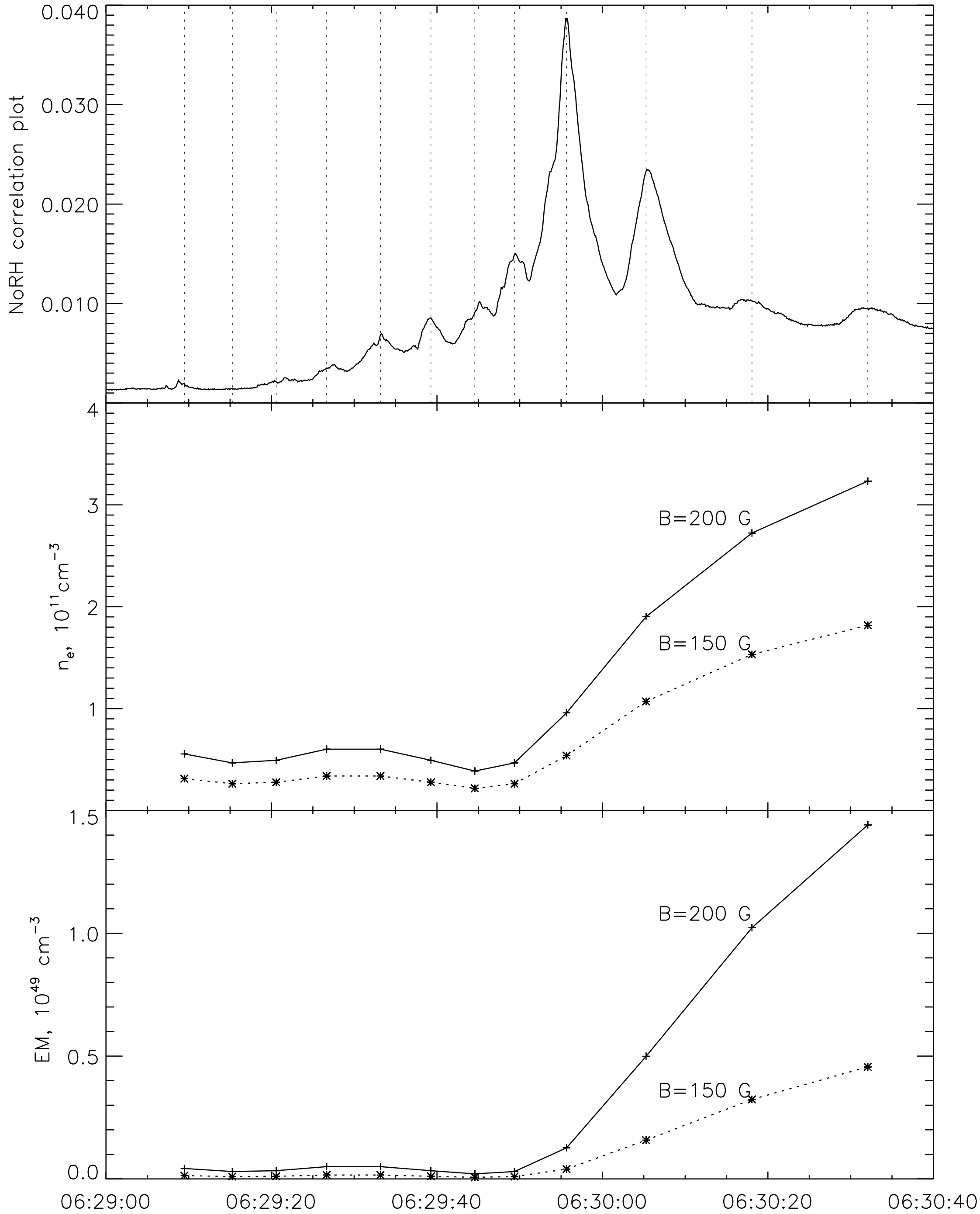

Fig. 10.— Oscillations in the time profile. Top: Oscillatory initial part of the total flux time profile at 17 GHz according to the NoRH correlation plot (time resolution 0.1 s). Peaks were found automatically with subsequent manual correction. Middle: variations of plasma density derived from the oscillations for assumed B = 200 G (solid) and 150 G (dotted). Bottom: emission measure derived from the oscillations.

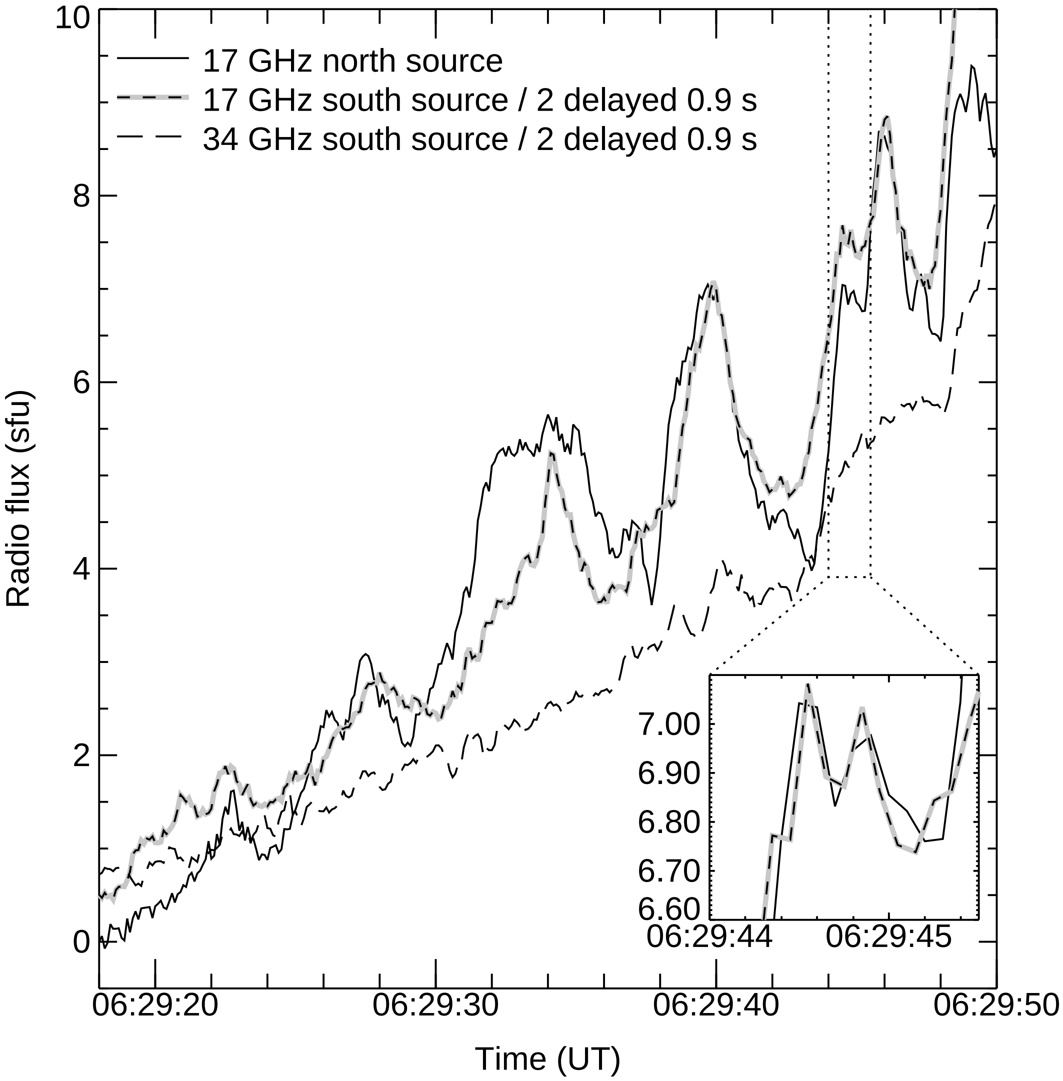

Fig. 11.— Comparison of the 17 GHz light curves for the main flare site ("southern" source, flux values divided by 2 to facilitate comparison) and the remote site ("northern" source) during the rise phase of the event. The light curve for the southern source has been delayed by 0.9 s in this figure to emphasize the similarity in the light curves, particularly in the period 06:29:37 – 06:29:48 UT. The time resolution of these data is 0.1 s. We also plot the 34 GHz light curve of the southern source, scaled by 0.5 and delayed as for the 17 GHz emission, but with a smoothing of 0.5 s applied to reduce the noise level. The 34 GHz emission of the southern source does not show the same level of fine structure as does the 17 GHz emission. The inset in the lower right of the panel shows a 1.5 s period from the two 17 GHz light curves in which the details match particularly well (the light curve for the main source has been shifted vertically to match that of the remote source). The delay of the main source relative to the remote source used in the inset is 0.95 s.